









Exceptional eruptive CO₂ emissions from intra-plate alkaline magmatism in the Canary volcanic archipelago

Mike Burton ^{1,2✉}, Alessandro Aiuppa ³, Patrick Allard ⁴, María Asensio-Ramos⁵, Ana Pardo Cofrades¹, Alessandro La Spina⁶, Emma J. Nicholson⁷, Vittorio Zanon ⁸, José Barrancos^{5,9}, Marcello Bitetto ³, Margaret Hartley ¹, Jorge E. Romero^{1,10}, Emma Waters ^{1,11}, Alex Stewart ¹, Pedro A. Hernández^{5,9}, João Pedro Lages^{3,7}, Eleazar Padrón ^{5,9}, Kieran Wood¹², Benjamin Esse¹, Catherine Hayer¹, Klaudia Cyrzan⁸, Estelle F. Rose-Koga ¹³, Federica Schiavi¹⁴, Luca D'Auria^{5,9} & Nemesio M. Pérez^{5,9}

Alkaline mafic magmas forming intra-plate oceanic islands are believed to be strongly enriched in CO₂ due to low-degree partial melting of enriched mantle sources. However, until now, such CO₂ enhancement has not been verified by measuring CO₂ degassing during a subaerial eruption. Here, we provide evidence of highly CO₂-rich gas emissions during the 86-day 2021 Tajogaite eruption of Cumbre Vieja volcano on La Palma Island, in the Canary archipelago. Our results reveal sustained high plume CO₂/SO₂ ratios, which, when combined with SO₂ fluxes, melt inclusion volatile contents and magma production rates at explosive and effusive vents, imply a magmatic CO₂ content of 4.5 ± 1.5 wt%. The amount of CO₂ released during the 2021 eruptive activity was 28 ± 14 Mt CO₂. Extrapolating to the volume of alkaline mafic magmas forming La Palma alone (estimated as 4000 km³ erupted over 11 Ma), we infer a maximum CO₂ emission into the ocean and atmosphere of 10¹⁶ moles of CO₂, equivalent to 20% of the eruptive CO₂ emissions from a large igneous province eruption, suggesting that the formation of the Canary volcanic archipelago produced a CO₂ emission of similar magnitude as a large igneous province.

¹ Department of Earth and Environmental Sciences, University of Manchester, Manchester, UK. ² Centre for the Observation and Modelling of Earthquakes, Volcanoes and Tectonics (COMET), Nottingham, UK. ³ Università degli Studi di Palermo, Dipartimento di Scienze della Terra e del mare, Palermo, Italy. ⁴ Université Paris Cité, Institut de Physique du Globe de Paris, Paris, France. ⁵ Instituto Volcanológico de Canarias (INVOLCAN), 38320 San Cristóbal de La Laguna, Tenerife, Canary Islands, Spain. ⁶ Istituto Nazionale di Geofisica e Vulcanologia, Sezione di Catania, Italy. ⁷ University College London, Earth Sciences, London, UK. ⁸ Instituto de Investigação em Vulcanologia e Avaliação de Riscos (IVAR), universidade dos Açores, Ponta Delgada, Portugal. ⁹ Instituto Tecnológico y de Energías Renovables (ITER), 38600 Granadilla de Abona, Tenerife, Canary Islands, Spain. ¹⁰ Instituto de Ciencias de la Ingeniería, Universidad de O'Higgins, Rancagua, Chile. ¹¹ School of Geographical & Earth Sciences, University of Glasgow, Glasgow, UK. ¹² University of Manchester, Department of Mechanical Aerospace and Civil Engineering, Manchester, UK. ¹³ Institut des Sciences de la Terre d'Orléans (ISTO), CNRS, Orléans, France. ¹⁴ Laboratoire Magma et Volcans (LMV), Université Clermont-Auvergne, CNRS, IRD, OPGC, Clermont Ferrand, France. ✉email: mike.burton@manchester.ac.uk

Volatiles exsolution and expansion during magma ascent are the primary drivers of volcanic eruptions¹ and volcanic gas emissions have had a profound impact on volatile cycles² and climate³ throughout Earth's history. Quantifying the volatile content of magmas is therefore a key objective in volcanological research. Among the main volatile species carried by magmas (H₂O, CO₂, SO₂, HCl, HF), CO₂ is the least soluble and, therefore, the first to exsolve, even at pressures consistent with the mid- to lower crust. Volatile solubility behaviour is well-established for a wide range of magma compositions from experiments under various pressure and temperature conditions⁴; thermodynamics⁵ and microanalysis of dissolved volatiles in melt (glassy) droplets and fluid inclusions entrapped in crystals that form during magma storage and ascent^{6,7}. The low solubility of CO₂ drives exsolution prior to melt inclusion formation which, in addition to post-entrapment CO₂-loss to bubbles and bubble decrepitation upon ascent⁸, means that inclusion-measured CO₂ contents are lower limits for the initial CO₂ content⁶. CO₂-rich fluid inclusions trapped at high pressures^{9,10} show that a co-existing fluid phase may be present even at mantle depths if CO₂ abundances are high enough^{11,12}. In low viscosity magmatic systems CO₂ bubbles are able to migrate separately or/and accumulate as foams at structural discontinuities¹³, thus degassing larger magma volumes than those eventually erupted. In our present study, we propose a limited impact from such differential CO₂ degassing processes, as our measurements did not reveal large evolutions in CO₂ compositions during the course of the eruption.

Trace element ratios such as CO₂/Nb and CO₂/Ba can provide an alternative approach to constrain the potential range of initial magmatic CO₂ content^{14,15}. Uncertainties arise, however, from the large variability in these ratios due to mantle heterogeneity and melt mixing¹⁶. Syn-eruptive measurements of CO₂ emissions, while challenging to acquire, can provide robust information on pre-eruptive contents of CO₂ and other volatiles, when combined with measurements of magma eruption rate, SO₂ fluxes and the initial magma sulfur (S) content^{12,14,17}. Eruptive gas compositions are measurable either remotely, using open-path Fourier Transform infra-red (OP-FTIR) spectroscopy with molten lava as the radiation source^{18,19}, or in-situ, using Multi-GAS analysis of dilute gas plumes²⁰; see Methods. Scaling the X/SO₂ ratio, where X is the volatile of interest, to the SO₂ flux measured from the ground and space^{21–23} provides the mass flux of CO₂ and other components. Normalising these mass fluxes to the mass eruption rate (MER) of magma then allows initial volatile contents in the magma to be calculated²⁴.

One of the most significant recent discoveries in volcanology is that magmatic CO₂ contents may be much higher than initially thought^{25,26}. This observation has important implications for the contribution of volcanism to the global geological CO₂ budget^{27,28} and to global climate and mass-extinction events during large igneous province eruptions²⁹. In particular, alkaline mafic magmas have been highlighted as a main source of CO₂-rich volcanism^{30–32}, with those erupted at intra-plate oceanic islands believed to be especially enriched in CO₂ due to low-degree partial melting of enriched mantle sources¹². In the Canary volcanic archipelago, eastern Atlantic ocean, a high CO₂ content between 2.5 and 5 wt% was estimated in basanites from El Hierro volcano³². However, direct measurements of CO₂ emissions during eruption of such magmas still remain sparse and were hitherto non-existent for the Canary volcanic archipelago.

The 2021 Tajogaite eruption of the Cumbre Vieja volcanic system, on La Palma island, provided a remarkable opportunity to quantify volatile emissions and magma volatile contents for alkaline mafic magmatism in this archipelago. The Canary Islands

constitute the subaerial portions of a group of voluminous intraplate volcanoes that predominantly erupt alkaline magmas derived from a heterogeneous mantle source³³. The Cumbre Vieja volcanic system is currently the most active in the archipelago; however, gas emissions from its last eruption in 1971 were not measured, so the 2021 eruption provided the first opportunity to assess gas geochemistry during a subaerial eruption in the Canary Islands.

The 85-day-long Tajogaite eruption began on 19th September 2021 along a NNW-ESE fracture system ~930 m above sea level, just above urbanised areas (Fig. 1). The eruption rapidly built up a main volcanic cone (Tajogaite) that hosted several linearly-aligned and closely-spaced vents^{34–36}. Powerful lava fountaining

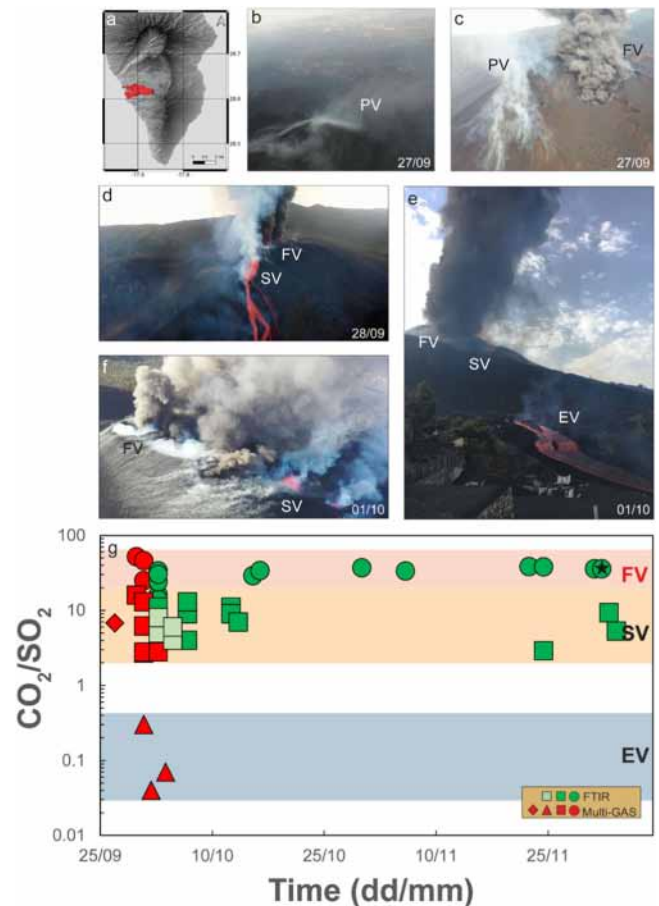


Fig. 1 The 2021 Tajogaite eruption (Cumbre Vieja, La Palma) and chronology of volcanic gas measurements. **a** The 2021 lava flow field in south-western La Palma. Aerial images of the near-vent eruptive region showing multiple distinct emission sources, eruptive styles, and degassing regimes (PV, passive vent; FV, fountaining vents; SV, spattering vent; EV, effusive vent). **b, c** Passive emissions during an eruptive pause and immediately following main vent reactivation on 27 September 2021. **d, e** Lateral progression in eruptive style from intense ash-producing lava fountaining activity at the upper vents (FV) through to spattering activity at the lower vent (SV), feeding lava flows; **f** Concurrent lava fountaining, spattering and non-explosive lava effusion on 1 October 2021. The EV opened at the base of the northern flank of the cone and fed lava extrusion for 2 days. **g** Temporal evolution of CO₂/SO₂ ratios in the gas plumes released by the different vents, as measured with Multi-GAS and OP-FTIR spectroscopy. Symbols indicate vent source (diamond = eruptive pause; circle = FV; square = SV (four especially water-rich compositions—see Fig. 2—are identified with light green tone); and triangle = EV). The star highlights the highest quality FV measurement.

and explosive activity were produced from central upper vents of the cone (referred to here as Fountaining Vent(s), FV), while spattering and lava flow effusion occurred at flank vents (hereafter referred to as Spattering Vent, SV, and Effusive Vent(s), EV; Fig. 1). Voluminous lava flows were erupted alongside sustained lava fountaining activity, producing dense lapilli and ash fallout, together forcing the evacuation of ~7000 people and caused extensive destruction until the end of the eruption on 13th December 2021³⁴. The initially erupted magma, an olivine-poor evolved basanite ascending from 10 to 16 km depth, was replaced by more primary, olivine-rich and highly oxidised basanite ascending from 27 to 31 km depth^{9,37,38}. Continuous syn-eruptive seismicity clustering at ~10–16 km and ~22–27 km³⁹, as well as the density distribution of CO₂-rich fluid inclusions in olivines^{9,38}, marked the respective storage depths of these two magmas.

The 2021 eruption site was relatively accessible, with established road/track infrastructure close to the vents. This enabled us to repeatedly (~daily) determine the chemical composition and mass flux of magmatic gases discharged from both explosive and effusive vents. Our measurements combined a suite of ground-based, aerial and orbital (satellite) instruments, locations are shown in Supplementary Fig. 1. Specifically, we quantified emitted gas compositions using Multi-GAS, deployed as ground-based (mobile and fixed stations) and drone-mounted systems, and OP-FTIR spectrometers (see Methods). We derived SO₂ fluxes using data from the satellite-based TROPOMI sensor (see Methods). In this study, we quantify the magmatic CO₂ flux produced during the 2021 Tajogaite eruption then combine with volcanological and petrological data to determine the CO₂ content of the basanitic magma.

Results

A key observation from our field measurements is the sharp, systematic contrast in CO₂/SO₂ ratios measured in gas emissions from the explosive upper vents (FV) and the spattering/effusive (SV/EV) flank vents (Fig. 1). This pattern is well-illustrated by Multi-GAS data obtained between 27 September and 3 October 2021, with CO₂/SO₂ molar ratios varying from 52–25 (FV) to 3–13 (SV) and down to 0.3–0.04 (EV), as well as by OP-FTIR data collected from 3 October until the end of the eruption (Supplementary Table 1 and Fig. 1). Such a spectacular compositional contrast, at vents only 500 m apart, demonstrates a predominant outgassing of poorly-soluble CO₂ through the central upper vents and, hence, its marked depletion in secondary degassing of the magma discharged effusively through the flank vents. A similar CO₂-fractionation pattern was previously documented on Mt. Etna between eruptive¹⁸ and passive degassing⁴⁰.

Our second key observation is that explosive gas emissions from the central upper vents (FV) displayed very high CO₂/SO₂ ratios during the whole eruption (Fig. 1). Our best OP-FTIR observations on December 2, 2021 (starred in Figs. 1 and 2) constrain the FV gas to contain 37 mol% H₂O, 61 mol% CO₂ and 1.7 mol% SO₂, with a CO₂/SO₂ molar ratio of 36 (24 by mass) (Supplementary Table 1). A similarly high CO₂/SO₂ ratio persisted at the FV throughout the entire eruption (Fig. 1), with a mean value of 33 ± 9.7 (or 23 ± 6.7 by mass). This makes the syn-eruptive gas from Tajogaite explosive vents one of the most CO₂-rich ever measured at an active volcano to date^{27,28,41}. By contrast, the mean CO₂/SO₂ ratio at the lower flank vents exhibiting lava spattering (SV) was 7.3 ± 4.0 (or 5.0 ± 2.7 by mass) throughout the eruption.

To reconstruct the magma degassing path(s) (Fig. 2), we measured the dissolved H₂O, CO₂, and S contents of glassy basanitic melt inclusions entrapped in erupted olivine crystals.

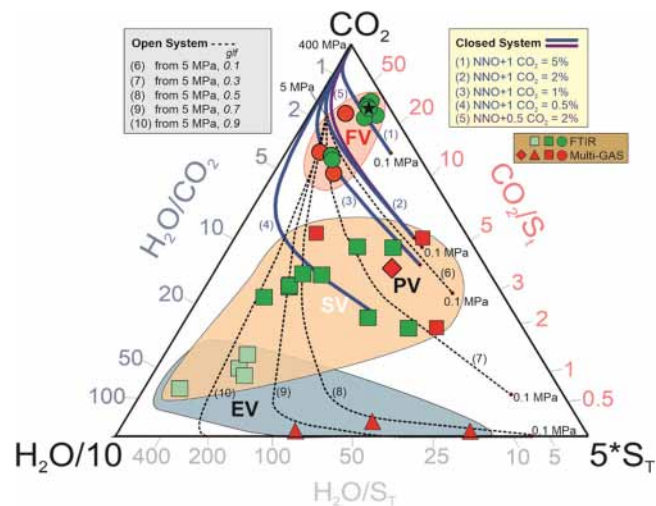


Fig. 2 Triangular plot showing H₂O, CO₂, and total sulfur (S_T) proportions in gas emissions from Tajogaite vents.

Gas emissions were measured both remotely (OP-FTIR) and directly (Multi-GAS). Upper fountaining vents (FV), spattering vent (SV) and effusive vents (EV) plot in distinct compositional fields. Symbol labelled PV corresponds to the Passively degassing Vent measured during an eruptive pause on 27 September 2021 (see Fig. 1 and Supplementary Data Table 1). Model degassing trends were computed for either closed- or open-system degassing using the solubility model of ref. [5]. Model runs are identified by numbers (Supplementary Data Table 3). For the open-system runs, we assume all the erupting magma goes towards the effusive vents at a branch point at 5 MPa while a variable proportion of the coexisting gas phase is transported to the explosive vent. Thus, a glf of 0.9 indicates a degassing pathway for magma, which lost 90% of its gas at 5 MPa to the explosive vent and then erupted at the effusive vent.

Details of volatile concentration measurement methods are shown below in “Methods” and in further detail in Supplementary Information. Dates and locations of sampling are shown in Supplementary Table 2 and dimensions of melt and fluid inclusions are in Supplementary Table 3. The sulphur content of these inclusions displays a narrow range, averaging 3290 ± 390 ppm (one standard deviation) and shows no systematic variation during the eruption (Supplementary Table 4 and Supplementary Figs. 2 and 3); it thus represents the initial sulphur abundance in the parental basanite. The same inclusions also contain 1.30–2.21 wt% H₂O and 0.22–0.50 wt% CO₂. According to experimental data for H₂O and CO₂ solubility in Canary basanites⁴², such concentrations correspond to melt inclusion entrapment pressures of ~290 to ~350 MPa, or ~10–12 km depth given the local crustal density structure³⁹. This depth range fits with the near-Moho seismogenic volume (at 10–16 km) active during the Cumbre Vieja eruption^{9,39}, which we interpret as an intermediate magma ponding zone fed by the more deeply sourced (15–27 km) basanite^{9,38}. The presence of pure CO₂ fluid inclusions in olivine and other crystals within the erupted magma^{9,38} indicate that the mantle-derived basanite already co-existed with a CO₂-rich gas phase prior to reaching this intermediate storage zone. It is thus very likely that the maximum dissolved CO₂ content in melt inclusions (0.50 wt%) underestimates the parental melt CO₂. Using a C-H-O-S solubility model⁵, we, therefore, computed the evolving fluid composition (Fig. 2 and Supplementary Fig. 4) during decompression of magma containing initial CO₂ contents of 0.5–5 wt%, in both closed- and open-system conditions, under temperature-redox conditions typical for La Palma basanites (see Methods; Supplementary Table 5).

Discussion

We interpret the gas composition data in the context of the distinct eruptive styles observed at the fountaining vents (FV) compared with spattering and effusive vents (SV and EV). In agreement with seismic evidence of rapid magma ascent from depth³⁸, we consider that magma and exsolved gas ascended rapidly in near closed-system up to a shallow branch point where gas-melt decoupling began. Most exsolved gas continued ascending vertically to fuel explosive fragmentation at the FV, whilst most of the magma was erupted at the SV and EV; this is a typical dynamic in low-viscosity scoria cone-forming eruptions⁴³. In this framework, the CO₂-rich gas emitted at the FV exsolved and last equilibrated at relatively high pressure, while the CO₂-poor, H₂O- and SO₂-richer gas emitted at the SV and EV derived primarily from low-pressure magma degassing of residual dissolved volatiles above the branch point.

Ultimately, the final gas compositions at FV, SV, and EV are controlled by the relative distributions of gas and magma between FV and EV/SV at the branch—which depends on geometry and fluid dynamics—and the dissolved concentration of SO₂ and H₂O remaining in the magma at the branch point. In Fig. 2, we assume that the branch point is at 10 MPa, ~400 m, and that all magma is erupted at the EV/SV (i.e. an end-member assumption).

Comparing our observations with modelled degassing trajectories in Fig. 2 shows that closed-system degassing with 0.5 wt% CO₂ (run 4) cannot reproduce the CO₂-rich FV compositions, confirming that maximum CO₂ concentrations measured in melt inclusions (0.5 wt%) underestimate the initial CO₂ abundance in the parental magma. FV compositions actually require closed-system degassing of a magma containing between 1 and 5 wt% initial CO₂ (runs 1–3, and 5) with gas and melt remaining in equilibrium until the inferred branch point between FV and SV/EV (Supplementary Fig. 4). In contrast, EV (and many SV) gas compositions can only be reproduced by open-system degassing from 5 MPa to atmospheric pressure.

An important result of our modelling is that the relatively oxidised melt^{9,37} favours a high S solubility, such that 90–95% of the initial sulphur is still dissolved at the branch point between FV and SV/EV (Supplementary Fig. 4b). The rapid magma ascent may have also limited the extent of gas exsolution. This result provides a critical control on the gas compositions produced at FV and SV/EV: it implies that the SO₂ flux produced at both FV and SV/EV was controlled largely by the mass eruption rate (MER) at each vent, whereas the CO₂ flux was predominantly emitted through FV as demonstrated by the much higher CO₂ content (CO₂/SO₂ ratio) of FV gas compared to SV/EV emissions. We highlight that the MER at the fountaining vents is critical to reproduce the high CO₂/SO₂ ratio in FV gas and, hence, to estimate the initial magma CO₂ content, in combination with the total MER, the total SO₂ flux and the initial S content. The calculations used to determine the initial CO₂ concentrations are provided in Supplementary Table 6, and the mass-balance approach we used is described below.

We quantify the total SO₂ flux using TROPOMI data collected from the Sentinel-5P satellite, analysed with a back-trajectory approach called PlumeTraj to determine the height, age and SO₂ mass in each pixel²³. Here we report the initial CO₂ content for two cases: (1) focusing on a particular measurement day, 3rd October 2021, when simultaneous Multi-GAS, FTIR and TROPOMI measurements were made, and (2) considering the integrated emissions and MERs for the entire eruption.

On 3rd October, there was strong and sustained explosive activity at the summit vents during the day, accompanied by voluminous lava effusion from SV and EV. Our TROPOMI/PlumeTraj measurements (Fig. 3) indicate that the average SO₂ flux was 860 ± 450 kg/s and the height of the eruption plume was

4500 ± 200 m, as confirmed by camera recording of the plume height from the Instituto Astrofísico de Canarias (IAC), 2365 m a.s.l. and 16.5 km north of the eruption⁴⁴. The height of Tajogaite cone was measured as 1100 m³⁵, so the net plume height was 3400 m. We quantify an explosive MER from this plume height of 22,600 ± 3300 kg/s using published scaling relationships⁴⁵. This is greater than the 9000 kg/s attributed to the mass eruption rate generating the tephra and cone deposit⁴⁴, with the difference arising from the mass of ash emitted into the atmosphere and transported more distally. Lava effusion rates were reported as 30 ± 15 m³/s on 3rd October⁴⁶, yielding an effusive MER of 78,500 ± 40,000 kg/s using the measured lava density of 2618 ± 179 kg/s⁴⁴.

The amount of sulphur released by unit mass of magma, ~3000 wt ppm, is given by the difference between the initial S content of 3290 ± 390 wt ppm measured in melt inclusions and the residual S content of the degassed glassy groundmass (440 wt ppm, which, corrected for the slight magma evolution during ascent, corresponds to 250 wt ppm whole rock). The key parameters described above (Supplementary Table 6) constrain much of the degassing system, but two key parameters remain to be defined: i) The quantity of SO₂ which had exsolved at the pressure of the branch point between effusive and explosive conduits, and ii) the percentage of total exsolved gas which was transferred to the explosive vents. There was ~200 m height difference between the effusive vents and the fountaining vents, but these probably joined even deeper within the system at the branch point. Here we estimate a 400 m depth or ~10 MPa pressure. According to the S solubility vs. pressure relationship shown in Supplementary Fig. 4b, only 5–10% of the initial S was exsolved at 10 MPa. This is an upper limit since fast magma ascent may have kinetically hampered gas exsolution. The percentage of exsolved gas entering the FV conduit can be estimated from volcanological observations. Because lava spattering at the SV was moderately vigorous and thus involved partly degassed magma, our best estimate is 84 ± 5% of the exsolved gas ascending directly to the FV and 16% carried to the SV and EV.

With 7.5% S exsolved at the branch point and 84% of exsolved gas entering the FV, we calculate that an initial CO₂ content of 4.4 ± 1.3 wt% is required to explain the CO₂/SO₂ mass ratio of 23 observed on 3rd October (see Fig. 4 and Supplementary Table 6). This produces an overall CO₂/SO₂ mass ratio for gas emissions from the effusive eruption of 1.7, which agrees with that measured in the mixed effusion/spattering gases (Fig. 1). The calculated SO₂ flux produced in this approach of 600 ± 300 kg/s matches the SO₂ flux of 860 ± 400 kg/s measured with TROPOMI (Fig. 3). We can do the same calculation using the time-averaged effusion and cone/tephra MERs, respectively assessed as 63,000 kg/s and 10,000 kg/s⁴⁴, and we estimate a similar magnitude MER for the total airborne ash emissions, producing 20,000 kg/s for the total explosive MER. The time-averaged SO₂ flux constrained by the TROPOMI-PlumeTraj data for the whole eruption is 500 ± 200 kg/s. With the same assumptions as above, we calculate an initial CO₂ content of 4.6 wt% and find excellent agreement between the calculated and observed average SO₂ flux. Overall, our mass balance approach leads to an initial magma CO₂ content ranging from 4.1 wt% to 5.9 wt% for a pre-exsolved SO₂ fraction of 5–10% and 80–95% exsolved gas entering the FV conduit. Our best estimate is 4.5 wt% (Fig. 4).

An initial CO₂ content of 4.5 wt% in the 2021 Tajogaite basanite matches the upper values of parental CO₂ content estimated for basanite erupted in 2011–2012 at nearby El Hierro island (2.5–4.2 wt%), based on dissolved/exsolved volatiles in melt inclusions and trace element ratios^{32,47}. A high CO₂ content in La Palma basanite is consistent with a low degree of partial melting of a mantle source metasomatized by recycled components, as also proposed for El Hierro magmas^{32,33,47}. For an initial magma CO₂ content of 4.5 wt% we infer a daily average emission rate of

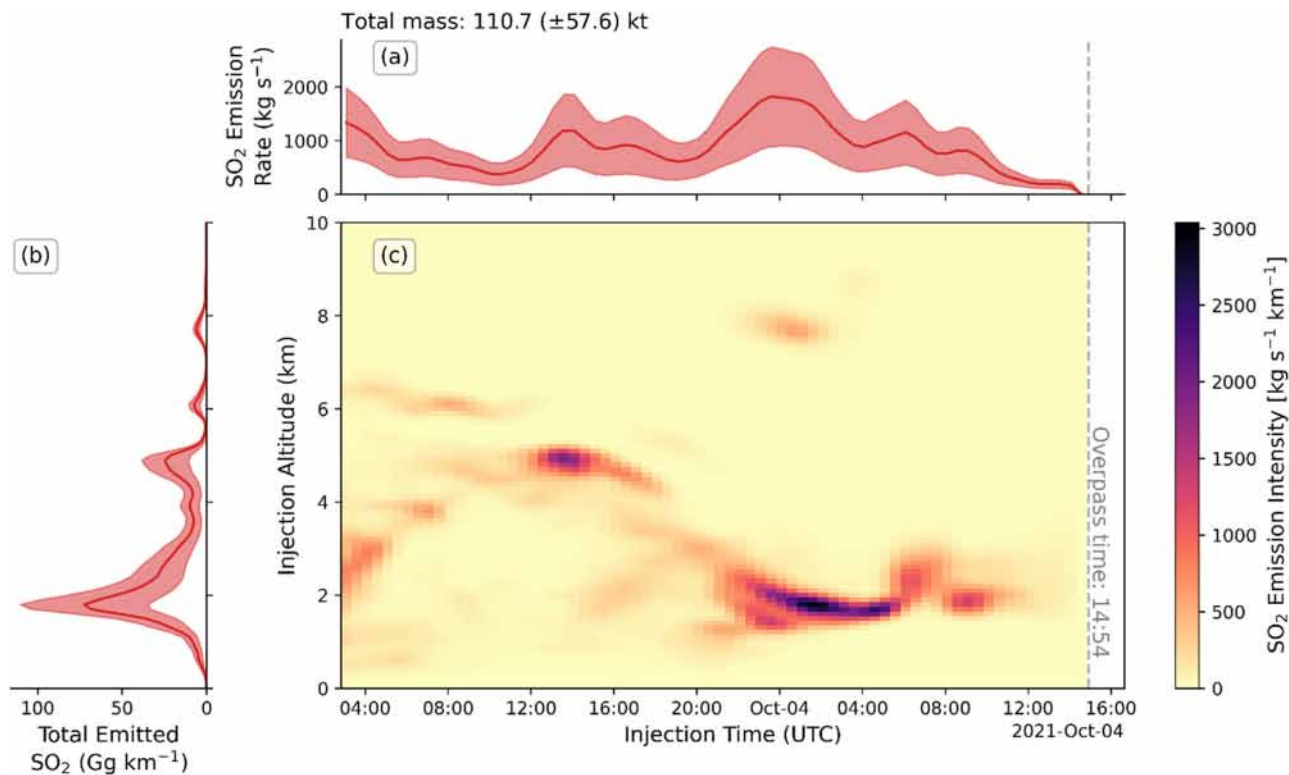


Fig. 3 Plume heights and fluxes retrieved from PlumeTraj/TROPOMI for 3-4 October 2021 during the 2021 Tajogaite eruption, La Palma. **a** SO_2 emission rate calculated over 36 h from a single TROPOMI SO_2 observation collected at 14:54 UTC on 4th October, by binning and integration of SO_2 from individual pixels in 10-min time bins. Errors reflect wind and SO_2 quantification uncertainty. 111 kt SO_2 over 36 h reflects an average SO_2 flux of 860 kg/s. **b** Height distribution of SO_2 emissions, dominated by a lower altitude persistent SO_2 emission from the lava field, and intermittent fountaining at the uppermost vents. **c** Emission intensity showing the evolution of SO_2 flux as a function of height and time.

$0.33 \pm 0.16 \text{ Mt d}^{-1}$ of CO_2 and an overall CO_2 emission of $28 \pm 14 \text{ Mt}$ during the 2021 Tajogaite eruption of Cumbre Vieja. This represents a large CO_2 emission compared to previously reported eruptive emissions at other volcanoes^{27,28,48}.

At the intermediate magma storage zone of ~10–15 km depth (ca. 275–410 MPa), where most of the syn-eruptive seismicity was occurring³⁹, CO_2 solubility in La Palma basanitic melts is predicted by solubility models⁴² to be only 0.25 to 0.6 wt%. Therefore, an important implication of our results is that about 4.0 wt% of CO_2 was already exsolved at these seismogenic depths, in agreement with observations of dense CO_2 -rich fluid inclusions^{9,38}. Under these conditions at least 1 wt% of H_2O may have coexisted with CO_2 in the exsolved fluid phase⁴². Thus, the basanitic magma stored at depths <27 km likely coexisted with an abundant exsolved fluid phase, which not only enhanced the explosivity of the eruption but could also increase the magma compressibility, buffering volumetric changes during depressurisation as the magma was erupted⁴⁹. We cannot exclude the possibility that pre-eruptive segregation and accumulation of this CO_2 -rich gas phase in a reservoir could have contributed to the eruptive gas emissions, thereby producing higher CO_2 contents in ascending magmas than that of the original stored magma. However, the preservation of high CO_2/SO_2 ratios in FV gas during the eruption suggests that there was not a strong differentiation of CO_2 within the feeding magma reservoir, and that therefore our quantification of magmatic CO_2 contents reflects that of the magma reservoir.

Conclusions

The volatile-rich nature of the 2021 Cumbre Vieja magma, particularly with respect to CO_2 , highlights that large-magnitude

volatile emissions can be produced by intraplate alkaline ocean volcanism from mantle sources previously enriched in recycled oceanic crust. This observation suggests that throughout Earth's history, the formation of ocean islands may have made a significant contribution to the geological carbon cycle. During the initial submarine formation of La Palma, there would have been substantial emission of volatiles into the ocean, followed by sub-aerial discharge once the island breached the surface. La Palma has a maximum height of 6423 m from ocean floor to summit and is, therefore, one of the tallest volcanic edifices on the planet. Its total submarine volume is estimated to be 3300 km^3 from topographic surveys^{50,51}. Its subaerial part is 1.7 Ma old and has a volume of 600 km^3 ^{52–54}, composed of a combination of gabbro, basanite and phonolite. Assuming for simplicity that basanite is the average composition of the entire edifice and initially contained 4.5 wt% CO_2 , we estimate a discharge of 68,000 Mt CO_2 (1.6×10^{15} moles) of CO_2 during La Palma's subaerial growth (Supplementary Table 7). If the submarine growth of La Palma volcanic island occurred at the same eruption rate as during its subaerial history, we then estimate a total build-up age of ~11 Ma and a total CO_2 production of ~480,000 Mt (1.1×10^{16} moles). This crude calculation likely provides an underestimate as it does not take into account the CO_2 contribution from intrusive magma emplacement into the crust. Such an amount of CO_2 is equivalent to ca. 20% of the estimated CO_2 release from a typical large igneous province²⁹, many of which are implicated in periods of major environmental and climatic change in Earth's history. Considering that La Palma is amongst the smaller of the eight main islands composing the Canary archipelago, we suggest that the integrated CO_2 emissions associated with the construction of the entire archipelago may approach that of an LIP.

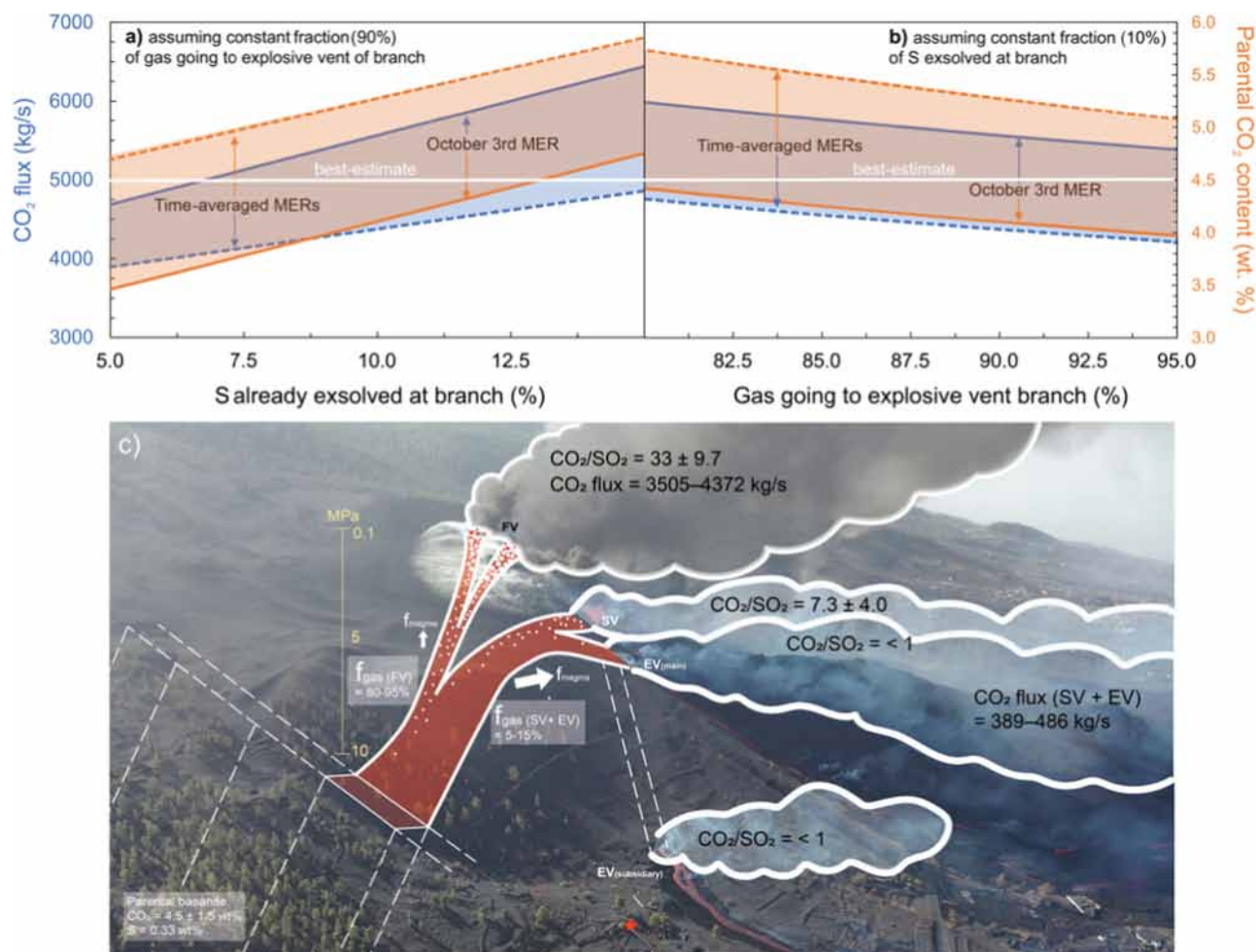


Fig. 4 Parental CO₂ content and total eruptive CO₂ flux computed from mass balance calculations (Supplementary Data Table 5). **a** This shows the range of variation of these two parameters when, at the branch point (about 10 MPa), the exsolved fraction of initial S is varied from 5 to 15% and 90% of the total exsolved at that point migrate in FV conduit. In **(b)** the latter is varied from 80 to 95%, while the exsolved fraction of initial S is kept constant at 10%. In both plots, the solid and dashed lines delineate the ranges in CO₂ content and flux obtained by considering magma eruption rates (MER) and SO₂ fluxes on October 3rd and for the entire eruption, respectively. **c** Photo of Tajogaite volcanic cone (drone flight on 2nd October) and schematic cross-section of the shallow (0.1–10 MPa) conduit system feeding FV, SV, and EV vents that best explains our observations and the above results. From about 10 MPa, the eruption feeder dyke [39] transitions into branched conduits where most of the CO₂-rich gas flux (f_{gas}) is preferentially channelled into subvertical FV conduit, sustaining powerful lava fountain, whereas magma influx (f_{magma}) predominantly concentrates through SV conduit then EV drains. The star points to our MultiGas and FTIR measuring site on 3rd October.

Methods

Volcanic gas composition. We measured plume gas composition during the Cumbre Vieja eruption using two independent and complementary techniques: in-situ plume measurements using aerial and ground-based Multi-GAS to characterise plume composition during the initial phase of the eruption (27 September to 4 October 2021) and remote sensing Fourier Transform Infra-red (FTIR) spectroscopy observations on 3 October to 2 December 2021 (Fig. 1). All gas composition results are listed in Supplementary Table 1.

Multi-GAS. The multi-component gas analyser system (Multi-GAS) technique was used to measure concentrations of CO₂, SO₂, H₂S ± H₂ (and P, T, RH) in the emitted gases. The Multi-GAS was operated as (a) a ground-based mobile instrument, (b) a ground-based fixed station, and (c) an aerial instrument, mounted onboard a DJI Matrice M210 quad-rotor Unoccupied Aerial System (UAS) platform (Supplementary Table 1). For all instruments, air is sampled through a 1 μm particle filter exposed to ambient air, at a pump rate of 1.0 L min⁻¹, and sensor data are

logged at 1 Hz. SO₂ and H₂S electrochemical sensors (T3ST/F and T3H, both City Technology) were calibrated for 0–200 and 0–200 ppmv, respectively, with an accuracy of ±2% and a resolution of 0.1 ppmv. A non-dispersive infra-red (NDIR) spectrometer—either a Microsensorik Smartgas Modul Premium2 (aerial Multi-GAS; 0–5000 ppm range) or a Edinburgh Gascard ND (ground-based Multi-GAS; 0–10,000 ppm range)—were calibrated for CO₂ with an accuracy of ±2% and a resolution of 1 ppmv. Units are shielded from radio frequency interference using a foil bag. Pressure (±1 hPa), temperature (±0.5 °C) and relative humidity (0–100%; ±3%) were also measured at 1 Hz using either a Bluedot BME280 sensor exposed to ambient air (aerial Multi-GAS) or Galltec sensor connected in series with the other sensors within the unit (ground-based).

UAS flights were undertaken in accordance with EU operating procedures, with airspace permission. Take-off locations were from two sites along Carretera San Nicolas, A (28.621302, -17.873859) and B (28.620874, -17.871741), each located ~900 m north of the summit vents (Supplementary Fig. 4). Flights involved between 30 and 1000 m of vertical ascent,

depending on the target vent emissions, and were between 10 and 20 min in duration—although typically only a fraction of that time was spent in the dense region of the gas plume.

We measured passive gas emissions during a pause in the eruption on 27 September 2021 from a position hovering several metres above the northern rim of the cone (labelled PV in Fig. 1b). The pause lasted several hours before the main upper vent reactivated with vigorous fountaining and ash emission (Fig. 1c), ~30 min after our sampling flight. The reactivation was preceded by the emission of a white steam-rich plume from the lower, spattering vent.

The gas plume from the main upper vents producing strong lava fountaining (labelled FV in Fig. 1) grounded towards the northwest of the cone on 30 September 2021. We measured the gas composition at a distance of ~900 m from the vent using a ground-based Multi-GAS operating in portable mode, by walking traverses through the plume. Subsequently, the unit was installed as a fixed, ground-based station and this remained in place until 2 October 2021 when the site became at risk from lava flows. The station was programmed to acquire data for 30 min every hour. The fixed station was exposed periodically to grounding plumes from both the upper, lava fountaining vents (FV) and lower, spattering vent (labelled SV in Fig. 1) and these two distinct emission sources produced resolvable CO₂/SO₂ ratios in the time series gas data. The gas emissions from the spattering vent (SV) were measured again on 3 October 2021 much closer to source using an aerial Multi-GAS unit on-board the UAS.

An effusive vent opened at the base of the northern flank of the cone overnight between 30 September and 1 October 2021 (labelled EV in Fig. 1f), producing a lava flow and a strong gas plume. We measured the gas composition from the effusive vent during a UAS flight on 1 October, a few tens of metres downwind from the vent and at around 30 m elevation above ground level. Subsequently, a second effusive vent opened at slightly higher elevation on the northern flank on 4 October 2021 and was again sampled using the UAS-mounted aerial Multi-GAS on the same day.

Multi-GAS instruments were calibrated with standard reference gases at University of Palermo, Italy, prior to and following the field campaign, but required no instrumental drift corrections. All sensor data are logged locally to a micro-SD card and, for the aerial Multi-GAS, also telemetered directly to the ground station (using a RFD 868x Modem by RFDdesign), where it can be viewed in real-time. The angle of the transmission antenna on the landing leg of the UAS required outwards orientation to minimise interference with the landing sensors located beneath the main body of the UAS. H₂O concentrations were calculated from records of temperature and relative humidity, using the ambient pressure at the measurement altitude, according to the Arden Buck equations relating the pressure of vapour saturation to temperature for moist air. We post-processed gas concentration time series using Ratiocalc software⁵⁵ and R. H₂S concentrations were corrected for the 13% cross-sensitivity of the sensor to SO₂ (determined during calibration with standard reference gases).

OP-FTIR. Two identical MIDAC OP-FTIR spectrometers with Stirling-cycle cooled MCT detectors were used to measure infrared absorption spectra of magmatic gas, sourced from the NERC Field Spectroscopy Facility (<https://fsf.nerc.ac.uk/>) and INGV Etna Observatory. We measured the compositions of magmatic gas produced by the eruptive vents and lava flows. The OP-FTIR is a very powerful and flexible instrument, and when performing absorption measurements can work wherever there is cooler magmatic gas observed in front of a warmer radiation source. We used it in both passive and solar absorption modes⁵⁶. Passive

measurements were conducted using incandescent ash eruption, lava fountaining and lava flow sources^{18,19,57–59}. Passive measurements provide constraints on H₂O, CO₂, SO₂ and HCl. FTIR spectra were analysed by fitting spectra created with the Reference Forward Model (<https://eodg.atm.ox.ac.uk/RFM/>) and HITRAN 2008 database⁶⁰. The fit windows were 2080–2150 cm⁻¹ for CO, CO₂ and H₂O, 2450–2550 cm⁻¹ for SO₂ and 2690–2830 for HCl.

FTIR observations were taken in various eruptive vents and activity styles from October 3 to December 4 (Supplementary Table 1). As an illustration, we detail our measurements on October 3, when we operated simultaneously two OP-FTIR spectrometers; a first one measured degassing from the main lava spattering flank vent (SV), from a distance of 0.7 km in the Tacande Village area, while the other was targeting the ash-rich eruptive column from summit vents (FV) from a distance of 3 km (Supplementary Fig. 1). Eruptive activity at the latter vents gradually increased in intensity as the measurements progressed, and we observed a mixed gas emission, partly arising from the SV and partly from the FV. Gas emissions from the SV clearly reflected a secondary, CO₂-depleted degassing stage of the magma, but still displaying a high CO₂/SO₂ molar ratio up to 11, plus SO₂/HCl = 8 and H₂O/SO₂ = 126. Explosive degassing from the FV showed variable compositions at different times, due to the changing conditions in ash content, eruption intensity, and interference with the drifting plume from the SV. Supplementary Table 1 lists the October 3 gas compositions measured successively during five intervals of ~10 min each. The increasing intensity of explosive activity during this sequence is reflected in an increasing cleanness of the chemical signature of the main summit degassing, with CO₂/SO₂ ratios increasing up to 33.6. On the evening of November 6, the eruptive activity shifted from ash-rich to Strombolian/lava fountaining, and we measured the lava fountain degassing from a distance of 5 km (dos Pinos area). We again recorded CO₂/SO₂ = 33.5. After a pause in explosive activity at the summit on 2nd December, a powerful sequence of continuous jetting of lava and gas started from a new vent cutting the NE flank of the grown main cone. We measured this sequence at 600 m from the vent, at Cabeza de Vaca, and obtained FTIR spectra with high signal-to-noise. The results further provided a high CO₂/SO₂ ratio of 35.8, with SO₂/HCl = 16.8 and H₂O/SO₂ = 22.4. This is our best compositional record of the FV eruptive plume.

Analyses of silicate melt inclusions and matrix glasses. We measured the volatile contents of olivine-hosted glassy melt inclusions and the groundmass glass of rapidly quenched air fall tephra. Major and minor elements plus sulfur, fluorine and chlorine in melt inclusions and matrix glasses were measured by electron microprobe in two independent laboratories in Paris (France) and Bristol University (UK). Analytical procedures are fully detailed in the Supplementary Information.

Melt inclusions, corrected for post-entrapment crystallisation, are basaltic in composition, and contain 40.2–46.4 wt% SiO₂, 2.8–4.5 wt% TiO₂, 4.4–6.3 wt% MgO and 1.1–2.1 wt% K₂O (Supplementary Fig. 1; Supplementary Table 2). Embayments and matrix glasses have more evolved and overlapping compositions, containing 43.0–49.5 wt% SiO₂, 1.4–4.1 wt% TiO₂, 0.8–5.3 wt% MgO, and 1.0–2.9 wt% K₂O (Supplementary Fig. 1). The olivines hosting melt inclusions and embayments have compositions between Fo₇₈ and Fo₈₅ (Supplementary Fig. 2). The mean melt inclusion S content is 3290 µg/g; one sulfur-rich inclusion contains 4,871 µg/g S, and the highest S content in the main melt inclusion population is 3715 µg/g (Supplementary Figs. 1 and 2). Groundmass glasses have a mean S content of 474 µg/g, indicating that ~85% of magmatic sulfur was outgassed

during magma ascent and eruption (Supplementary Information), as also tracked by glassy embayments trapped at the rim of crystals in comparison to sulfur, chlorine and fluorine show only minor outgassing during ascent: dissolved concentrations respectively vary from ca 450–1050 $\mu\text{g/g}$ Cl and 1000–1500 $\mu\text{g/g}$ F in melt inclusions, to ca. 1400 $\mu\text{g/g}$ Cl and 1000–1500 $\mu\text{g/g}$ F in groundmass glass and melt embayment (fluorine reaching up to 2200 $\mu\text{g/g}$ in one embayment). Fluorine and chlorine become progressively more enriched as melt inclusions and glass compositions become more evolved, indicating that melt F and Cl contents are primarily governed by a fractional crystallisation relationship. Embayments and groundmass glasses have similar F and Cl contents, suggesting that syn-eruptive F and Cl outgassing at the vents was inefficient. H_2O and CO_2 were determined in three melt inclusions only (Supplementary Table 2). Analysed groundmass glasses are tephritic in composition. They have degassed all their CO_2 and contain 520–1510 $\mu\text{g/g}$ residual H_2O .

Degassing modelling. We model the theoretical composition of the exsolved fluid phase in equilibrium with the La Palma basanite using a C-S-O-H saturation model⁵. This model (publicly available for download at <https://github.com/charlesll/chosetto>) has been applied before to other volcanoes with widely different magma compositions^{31,61–63}. Model runs are initialised for a range of starting conditions and over a range of pressures and redox conditions relevant to La Palma basanites (Supplementary Table 3). Details of all model runs are illustrated in Supplementary Table 3. Model runs are performed using as parental melt (major elements) a typical La Palma basanite. H_2O and S contents are from dissolved content in Cumbre Vieja melt inclusions (this study; Supplementary Table 2). CO_2 is assumed to vary from 1 to 5 wt% in the different model runs to reproduce the postulated range for primary melts in the Canary^{64,65}. All runs are performed by simulating isothermal (temperature kept constant at 1273 °K) magma decompression from an initial pressure of either 400 MPa (models (1) to (4)) or 5 MPa (models (5) to (9)) down to atmospheric conditions (0.1 MPa). Runs are performed under closed-system conditions (i.e., gas and melt continuously re-equilibrating during the decompression path) in runs (1) to (4) to simulate basanite ascent from source to shallow volcanic conduit. Runs (5) to (9) simulate the basanite degassing path in the shallow conduit, in which separated gas is allowed to freely escape from the melt (open system conditions). These models differ for the quantity (mass fraction) of gas removed at each pressure step, this “gas fraction lost” ranging from 0.1 (run (5)) to 0.9 (run (9)). In both closed and open system degassing, equilibrium compositions of the melt and the coexisting gas are calculated at each step throughout the decompression path. Redox conditions are fixed at 1 log units above the Nickel-Nickel Oxide (NNO) buffer ($\Delta\text{NNO} = +1$) to fit the oxidised nature of the La Palma melt³⁷ and intraplate alkaline melts in general⁶⁴. Run (4) uses slightly less oxidised redox conditions ($\Delta\text{NNO} = +0.5$) to explore the effect of redox on the degassing path. Comparison between results obtained in runs (2) and (4) suggests a 0.5 log unit change in redox has limited role in the degassing paths (Fig. 2). In all model runs, the equilibrium exsolved gas varies during the degassing path from CO_2 -rich at high pressure to H_2O -S-rich at low pressure (Fig. 2). The pressure-dependent evolution of the modelled $\text{CO}_2/\text{S}_\text{T}$ ratios is illustrated in Supplementary Fig. 3. From this, we infer that the FV gas corresponds to the equilibrium gas at 1–3 MPa in runs (1) to (4), implying closed system degassing conditions likely prevailed until very shallow in the upper conduits. The largest CO_2 depletions are observed in open system and at low pressure, such conditions reproducing well the CO_2 -poor compositions of EV gases (Fig. 2 and Supplementary

Fig. 3). The modelled dissolved S contents (Supplementary Fig. 4) also imply that S degassing from melt becomes significant only at very shallow levels (<10 MPa). The predicted dissolved S content at atmospheric pressure (0.1 MPa) matches closely the mean groundmass glass S content of 474 ppm (Supplementary Fig. 4).

SO_2 flux and plume height. TROPOMI data were analysed with the PlumeTraj approach^{66–69}, in which back-trajectory analysis is applied to determine the height at which gas would have needed to have been injected into the atmosphere above Cumbre Vieja to arrive at the observed pixel location. The height constraints then allow correction of the retrieved SO_2 masses. This is critical because the sensitivity of TROPOMI to SO_2 is strongly height dependent, meaning that without an accurate quantification of plume height SO_2 masses cannot be accurately quantified. Errors on the retrieved height and SO_2 mass are determined using the size of each pixel, the reported retrieved SO_2 mass error and the meteorological wind field error. Pixel heights and masses are then distributed in 10 min time bins, combining uncertainties from each pixel’s contribution to a time bin in quadrature. This produces a time series of SO_2 flux density, the distribution of SO_2 mass as a function of height and time. The initial motivation for retrieving plume height is to correct the retrieved SO_2 mass, but it is also an extremely valuable measurement, reflecting the evolution of the explosive mass eruption rate. The intense degassing during the first two weeks of the Cumbre Vieja eruption permitted the quantification of gas emissions emitted up to 36–48 h prior to image collection, providing complete and continuous temporal coverage of the plume height and SO_2 emission rate. This was particularly valuable in the early stage of the eruption before ground-based measurements could be deployed.

Data availability

All data reported in the paper are listed in Supplementary Tables. Melt inclusion data are available as Supplementary Dataset 1 and on figshare: <https://doi.org/10.6084/m9.figshare.24442444.v1>.

Code availability

The solubility model code is available here: <https://github.com/charlesll/chosetto>.

Received: 17 May 2023; Accepted: 13 November 2023;

Published online: 12 December 2023

References

1. Sparks, R. S. J. Forecasting volcanic eruptions. *Earth Planet. Sci. Lett.* **210**, 1–15 (2003).
2. Jambon, A. Earth degassing and large-scale geochemical cycling of volatile elements. *Volatiles Magmas* **30**, 479–517 (1994).
3. Ernst, R. E. & Youbi, N. How Large Igneous Provinces affect global climate, sometimes cause mass extinctions, and represent natural markers in the geological record. *Palaeogeogr. Palaeoclimatol. Palaeoecol.* **478**, 30–52 (2017).
4. Eguchi, J. & Dasgupta, R. A CO_2 solubility model for silicate melts from fluid saturation to graphite or diamond saturation. *Chem. Geol.* **487**, 23–38 (2018).
5. Moretti, R., Papale, P. & Ottonello, G. A model for the saturation of C-O-H-S fluids in silicate melts. *Volcan. Degassing* **213**, 81–101 (2003).
6. Hartley, M. E., Maclennan, J., Edmonds, M. & Thordarson, T. Reconstructing the deep CO_2 degassing behaviour of large basaltic fissure eruptions. *Earth Planet. Sci. Lett.* **393**, 120–131 (2014).
7. Metrich, N. & Wallace, P. J. Minerals, inclusions and volcanic processes. *Reviews in Mineralogy & Geochemistry, Mineralogical Society of America*. Vol. 69 (eds Putirka, K. D. & Tepley, F. J.) 363–402 (2008).
8. Maclennan, J. Bubble formation and decrepitation control the CO_2 content of olivine-hosted melt inclusions. *Geochem. Geophys. Geosyst.* **18**, 597–616 (2017).
9. Dayton, K. et al. Deep magma storage during the 2021 La Palma eruption. *Sci. Adv.* **9**, eade7641 (2023).

10. Hansteen, T. H., Klugel, A. & Schmincke, H. U. Multi-stage magma ascent beneath the Canary Islands: evidence from fluid inclusions. *Contrib. Miner. Petrol.* **132**, 48–64 (1998).
11. Longpre, M. A., Klugel, A., Diehl, A. & Stix, J. Mixing in mantle magma reservoirs prior to and during the 2011–2012 eruption at El Hierro, Canary Islands. *Geology* **42**, 315–318 (2014).
12. Spilliaert, N., Allard, P., Metrich, N. & Sobolev, A. V. Melt inclusion record of the conditions of ascent, degassing, and extrusion of volatile-rich alkali basalt during the powerful 2002 flank eruption of Mount Etna (Italy). *J. Geophys. Res.-Solid Earth* **111** <https://doi.org/10.1029/2005jb003934> (2006).
13. Jaupart, C. & Vergnolle, S. The generation and collapse of a foam layer at the roof of a basaltic magma chamber. *J. Fluid Mech.* **203**, 347–380 (1989).
14. Aiuppa, A., Casetta, F., Coltorti, M., Stagno, V. & Tamburello, G. Carbon concentration increases with depth of melting in Earth's upper mantle. *Nat. Geosci.* **14**, 697 (2021).
15. Saal, A. E., Hauri, E. H., Langmuir, C. H. & Perfit, M. R. Vapour undersaturation in primitive mid-ocean-ridge basalt and the volatile content of Earth's upper mantle. *Nature* **419**, 451–455 (2002).
16. Matthews, S., Shorttle, O., Rudge, J. F. & MacLennan, J. Constraining mantle carbon: CO₂-trace element systematics in basalts and the roles of magma mixing and degassing. *Earth Planet. Sci. Lett.* **480**, 1–14 (2017).
17. Burton, M. R., Mader, H. M. & Polacci, M. The role of gas percolation in quiescent degassing of persistently active basaltic volcanoes. *Earth Planet. Sci. Lett.* **264**, 46–60 (2007).
18. Allard, P., Burton, M. & Mure, F. Spectroscopic evidence for a lava fountain driven by previously accumulated magmatic gas. *Nature* **433**, 407–410 (2005).
19. Burton, M., Allard, P., Mure, F. & La Spina, A. Magmatic gas composition reveals the source depth of slug-driven Strombolian explosive activity. *Science* **317**, 227–230 (2007).
20. Aiuppa, A. et al. Total volatile flux from Mount Etna. *Geophys. Res. Lett.* **35** <https://doi.org/10.1029/2008gl035871> (2008).
21. Galle, B. et al. A miniaturised ultraviolet spectrometer for remote sensing of SO₂ fluxes: a new tool for volcano surveillance. *J. Volcanol. Geotherm. Res.* **119**, 241–254 (2003).
22. Carn, S. A., Fioletov, V. E., McLinden, C. A., Li, C. & Krotkov, N. A. A decade of global volcanic SO₂ emissions measured from space. *Sci. Rep.* **7** <https://doi.org/10.1038/srep44095> (2017).
23. Burton, M., Hayer, C., Miller, C. & Christenson, B. Insights into the 9 December 2019 eruption of Whakaari/White Island from analysis of TROPOMI SO₂ imagery. *Sci. Adv.* **7** <https://doi.org/10.1126/sciadv.abg1218> (2021).
24. Pardini, F., Burton, M., Arzilli, F., La Spina, G. & Polacci, M. SO₂ emissions, plume heights and magmatic processes inferred from satellite data: the 2015 Calbuco eruptions. *J. Volcanol. Geotherm. Res.* **64232**, 13 (2018).
25. Anderson, K. R. & Poland, M. P. Bayesian estimation of magma supply, storage, and eruption rates using a multiphysical volcano model: Kilauea Volcano, 2000–2012. *Earth Planet. Sci. Lett.* **447**, 161–171 (2016).
26. Blundy, J., Cashman, K. V., Rust, A. & Witham, F. A case for CO₂-rich arc magmas. *Earth Planet. Sci. Lett.* **290**, 289–301 (2010).
27. Werner, C. et al. Carbon dioxide emissions from subaerial volcanic regions two decades in review. *Deep Carbon: Past to Present.* (eds Orcutt, B. N., Daniel, I. & Dasgupta, R.) 188–236 (Cambridge University Press, 2020).
28. Burton, M. R., Sawyer, G. M. & Granieri, D. Deep carbon emissions from volcanoes. *Carbon Earth* **75**, 323–354 (2013).
29. Mills, B., Daines, S. J. & Lenton, T. M. Changing tectonic controls on the long-term carbon cycle from Mesozoic to present. *Geochem. Geophys. Geosyst.* **15**, 4866–4884 (2014).
30. Allard, P. et al. Eruptive and diffuse emissions of CO₂ from Mount Etna. *Nature* **351**, 387–391 (1991).
31. Oppenheimer, C. et al. Mantle to surface degassing of alkalic magmas at Erebus volcano, Antarctica. *Earth Planet. Sci. Lett.* **306**, 261–271 (2011).
32. Longpre, M. A., Stix, J., Klugel, A. & Shimizu, N. Mantle to surface degassing of carbon- and sulphur-rich alkaline magma at El Hierro, Canary Islands. *Earth Planet. Sci. Lett.* **460**, 268–280 (2017).
33. Day, J. M. D., Pearson, D. G., Macpherson, C. G., Lowry, D. & Carracedo, J. C. Evidence for distinct proportions of subducted oceanic crust and lithosphere in HIMU-type mantle beneath El Hierro and La Palma, Canary Islands. *Geochim. Cosmochim. Acta* **74**, 6565–6589 (2010).
34. Romero, J. E. et al. The initial phase of the 2021 Cumbre Vieja ridge eruption (Canary Islands): products and dynamics controlling edifice growth and collapse. *J. Volcanol. Geotherm. Res.* **431** <https://doi.org/10.1016/j.jvolgeores.2022.107642> (2022).
35. Civico, R. et al. High-resolution digital surface model of the 2021 eruption deposit of Cumbre Vieja volcano, La Palma, Spain. *Sci. Data* **9** <https://doi.org/10.1038/s41597-022-01551-8> (2022).
36. Bonadonna, C., Folch, A., Loughlin, S. & Puempel, H. Future developments in modelling and monitoring of volcanic ash clouds: outcomes from the first IAVCEI-WMO workshop on Ash Dispersal Forecast and Civil Aviation. *Bull. Volcanol.* **74**, 1–10 (2012).
37. Day, J. M. D. et al. Mantle source characteristics and magmatic processes during the 2021 La Palma eruption. *Earth Planet. Sci. Lett.* **597** <https://doi.org/10.1016/j.epsl.2022.117793> (2022).
38. Zanon, V. et al. in *EGU General Assembly 2022* (Copernicus, Vienna, Austria, 2022).
39. D'Auria, L. et al. Rapid magma ascent beneath La Palma revealed by seismic tomography. *Sci. Rep.* **12** <https://doi.org/10.1038/s41598-022-21818-9> (2022).
40. La Spina, A., Burton, M. & Salerno, G. G. Unravelling the processes controlling gas emissions from the central and northeast craters of Mt. Etna. *J. Volcanol. Geotherm. Res.* **198**, 368–376 (2010).
41. Aiuppa, A., Fischer, T. P., Plank, T., Robidoux, P. & Di Napoli, R. Along-arc, inter-arc and arc-to-arc variations in volcanic gas CO₂/S-T ratios reveal dual source of carbon in arc volcanism. *Earth-Sci. Rev.* **168**, 24–47 (2017).
42. Jimenez-Mejias, M., Andujar, J., Scaillet, B. & Casillas, R. Experimental determination of H₂O and CO₂ solubilities of mafic alkaline magmas from Canary Islands. *Comptes Rendus Geosci.* **353**. <https://doi.org/10.5802/crgeos.84> (2021).
43. Pioli, L., Azzopardi, B. J. & Cashman, K. V. Controls on the explosivity of scoria cone eruptions: Magma segregation at conduit junctions. *J. Volcanol. Geotherm. Res.* **186**, 407–415 (2009).
44. Bonadonna, C. et al. Physical characterization of long-lasting hybrid eruptions: the 2021 Tajogaite eruption of Cumbre Vieja (La Palma, Canary Islands). *J. Geophys. Res.-Solid Earth* **127** <https://doi.org/10.1029/2022jb025302> (2022).
45. Mastin, L. G. et al. A multidisciplinary effort to assign realistic source parameters to models of volcanic ash-cloud transport and dispersion during eruptions. *J. Volcanol. Geotherm. Res.* **186**, 10–21 (2009).
46. Plank, S. et al. Combining thermal, tri-stereo optical and bi-static InSAR satellite imagery for lava volume estimates: the 2021 Cumbre Vieja eruption, La Palma. *Sci. Rep.* **13**, 2057 (2023).
47. Taracsak, Z. et al. High fluxes of deep volatiles from ocean island volcanoes: insights from El Hierro, Canary Islands. *Geochim. Cosmochim. Acta* **258**, 19–36 (2019).
48. Aiuppa, A., Fischer, T. P., Plank, T. & Bani, P. CO₂ flux emissions from the Earth's most actively degassing volcanoes, 2005–2015. *Sci. Rep.* **9**. <https://doi.org/10.1038/s41598-019-41901-y> (2019).
49. Kilbride, B. M., Edmonds, M. & Biggs, J. Observing eruptions of gas-rich compressible magmas from space. *Nat. Commun.* **7**. <https://doi.org/10.1038/ncomms13744> (2016).
50. Masson, D. G. et al. Slope failures on the flanks of the western Canary Islands. *Earth-Sci. Rev.* **57**, 1–35 (2002).
51. Mitchell, N. C., Masson, D. G., Watts, A. B., Gee, M. J. R. & Urgeles, R. The morphology of the submarine flanks of volcanic ocean islands—a comparative study of the Canary and Hawaiian hotspot islands. *J. Volcanol. Geotherm. Res.* **115**, 83–107 (2002).
52. Guillou, H., Carracedo, J. C. & Duncan, R. A. K-Ar, 40Ar-39Ar ages and magnetostratigraphy of Brunhes and Matuyama lava sequences from La Palma Island. *J. Volcanol. Geotherm. Res.* **106**, 175–194 (2001).
53. Staudigel, H. & Schmincke, H. U. The pliocene seamount series of la palma Canary-Islands. *J. Geophys. Res.* **89**, 1195–1215 (1984).
54. Staudigel, H., Feraud, G. & Giannerini, G. The history of intrusive activity on the island of la-palma (Canary-Islands). *J. Volcanol. Geotherm. Res.* **27**, 299–322 (1986).
55. Tamburello, G. Ratiocalc: software for processing data from multicomponent volcanic gas analyzers. *Comput. Geosci.* **82**, 63–67 (2015).
56. Francis, P., Burton, M. R. & Oppenheimer, C. Remote measurements of volcanic gas compositions by solar occultation spectroscopy. *Nature* **396**, 567–570 (1998).
57. Pfeffer, M. A. et al. Ground-based measurements of the 2014–2015 Holuhraun volcanic cloud (Iceland). *Geosciences* **8**. <https://doi.org/10.3390/geosciences8010029> (2018).
58. La Spina, A., Burton, M., Allard, P., Alparone, S. & Mure, F. Open-path FTIR spectroscopy of magma degassing processes during eight lava fountains on Mount Etna. *Earth Planet. Sci. Lett.* **413**, 123–134 (2015).
59. La Spina, A. et al. New insights into volcanic processes at Stromboli from Cerberus, a remote-controlled open-path FTIR scanner system. *J. Volcanol. Geotherm. Res.* **249**, 66–76 (2013).
60. Rothman, L. S. et al. The HITRAN2012 molecular spectroscopic database. *J. Quant. Spectrosc. Radiat. Transfer* **130**, 4–50 (2013).
61. de Moor, J. M. et al. Turmoil at Turrialba Volcano (Costa Rica): degassing and eruptive processes inferred from high-frequency gas monitoring. *J. Geophys. Res.-Solid Earth* **121**, 5761–5775 (2016).
62. Moretti, R. et al. The 2018 unrest phase at La Soufriere of Guadeloupe (French West Indies) andesitic volcano: Scrutiny of a failed but prodromal phreatic eruption. *J. Volcanol. Geotherm. Res.* **393**. <https://doi.org/10.1016/j.jvolgeores.2020.106769> (2020).

63. Moretti, R. & Papale, P. On the oxidation state and volatile behavior in multicomponent gas-melt equilibria. *Chem. Geol.* **213**, 265–280 (2004).
64. Taracsak, Z. et al. Highly Oxidising Conditions in Volatile-Rich El Hierro Magmas: implications for Ocean Island Magmatism. *J. Petrol.* **63**. <https://doi.org/10.1093/petrology/egac011> (2022).
65. Longpre, M. A. & Felpeo, A. Historical volcanism in the Canary Islands; part 1: a review of precursory and eruptive activity, eruption parameter estimates, and implications for hazard assessment. *J. Volcanol. Geotherm. Res.* **419**. <https://doi.org/10.1016/j.jvolgeores.2021.107363> (2021).
66. Hayer, C., Burton, M., Ferrazzini, V., Esse, B. & Di Muro, A. Unusually high SO₂ emissions and plume height from Piton de la Fournaise volcano during the April 2020 eruption. *Bull. Volcanol.* **85**, 21 (2023).
67. Esse, B. et al. Satellite-derived SO₂ emissions from the relatively low-intensity, effusive 2021 eruption of Fagradalsfjall, Iceland. *Earth Planet. Sci. Lett.* **619**. <https://doi.org/10.1016/j.epsl.2023.118325> (2023).
68. Queisser, M. et al. TROPOMI enables high-resolution SO₂ flux observations from Mt. Etna, Italy, and beyond. *Sci. Rep.* **9** <https://doi.org/10.1038/s41598-018-37807-w> (2019).
69. Pardini, F. et al. Initial constraints on triggering mechanisms of the eruption of Fuego volcano (Guatemala) from 3 June 2018 using IASI satellite data. *J. Volcanol. Geotherm. Res.* **376**, 54–61 (2019).

Acknowledgements

M.B., B.E. and C.H. gratefully acknowledge funding support from UKRI NERC VPLUS, grant NE/S004106/1. We are very grateful to the NERC Field Spectroscopy Facility <https://fsf.nerc.ac.uk/> for the loan of an FTIR spectrometer and support in the field. J.R. was supported by the University of Manchester's Deans Doctoral Award. J.R.A.A., M.Bitetto and J.P.L. received funding from the Italian Ministero Università Ricerca (MUR, Projects PRIN2017LMNLAW and PRIN2022HA8XCS), and from the RETURN Extended Partnership funded by the European Union Next-Generation EU (National Recovery and Resilience Plan – NRRP, Mission 4, Component 2, Investment 1.3 – D.D. 1243 2/8/2022, PE0000005). M.A.-R., J.B., P.A.H., E.P., L.D. and N.M.P. received funding from the projects VOLRISKMAC II (MAC2/3.5b/328), co-financed by the EC Cooperation Transnational Program MAC 2014–2020, “Cumbre Vieja Emergencia”, financed by the Spanish Ministry of Science and Innovation, TFassistance financed by Cabildo Insular de Tenerife and LPvolcano financed by the Cabildo Insular de La Palma. This work has been partially funded by the Fundação para a Ciência e Tecnologia (FCT), Portugal, through project MAGAT project (Ref. CIRCNA/OCT/2016/2019).

Author contributions

MB led the production and writing of the paper, interpretations and modelling were developed by M.B., A.A., P.A., M.A.-R., A.P.C., A.L.S., E.J.N. and V.Z. who also

contributed to writing the paper. FTIR data were collected and analysed by M.A.-R., A.P.C., A.L.S., M.B., P.A. and J.B. Multigas and SO₂ camera data were collected by A.A., E.J.N., M.Bitetto, J.P.L., E.P. and K.W. TROPOMI SO₂ fluxes were produced by C.H., B.E. and M.B. Melt inclusion measurements were performed by M.H., V.Z., A.S., E.W., K.C., J.R., E.F.R.-K. and F.S. P.A.H., L.D. and N.M.P. provided helped plan the field activity and provide logistical and scientific support which allowed fieldwork to be conducted safely during the eruption.

Competing interests

E.J.N. is an Editorial Board Member for Communications Earth & Environment, but was not involved in the editorial review of, nor the decision to publish, this article. All other authors declare no competing interests.

Additional information

Supplementary information The online version contains supplementary material available at <https://doi.org/10.1038/s43247-023-01103-x>.

Correspondence and requests for materials should be addressed to Mike Burton.

Peer review information *Communications Earth & Environment* thanks Thor Hansteen and Ramón Casillas for their contribution to the peer review of this work. Primary Handling Editor Joe Aslin. A peer review file is available.

Reprints and permission information is available at <http://www.nature.com/reprints>

Publisher's note Springer Nature remains neutral with regard to jurisdictional claims in published maps and institutional affiliations.



Open Access This article is licensed under a Creative Commons Attribution 4.0 International License, which permits use, sharing, adaptation, distribution and reproduction in any medium or format, as long as you give appropriate credit to the original author(s) and the source, provide a link to the Creative Commons licence, and indicate if changes were made. The images or other third party material in this article are included in the article's Creative Commons licence, unless indicated otherwise in a credit line to the material. If material is not included in the article's Creative Commons licence and your intended use is not permitted by statutory regulation or exceeds the permitted use, you will need to obtain permission directly from the copyright holder. To view a copy of this licence, visit <http://creativecommons.org/licenses/by/4.0/>.

© The Author(s) 2023